**Proceedings of the ASME 2020**
**Verification and Validation Symposium**
**VVS2020**
**May 20-22, 2020, Virtual, Online**

**VVS2020-8808**

# VERIFICATION OF A NUMERICAL MODEL FOR SIMULATING INTERVERTEBRAL DISC PATHOPHYSIOLOGY

**Xin Gao**
SilicoSpine Inc., Miami, FL

**Weiyong Gu**[1]
University of Miami, Coral Gable, FL
SilicoSpine Inc., Miami, FL



## ABSTRACT

Intervertebral disc (IVD) degeneration may cause low back pain which has a tremendous impact on the society and economy in the United States. It is important to quantitatively and qualitatively evaluate its pathophysiology in order to diagnose and treat disc degeneration. Recently, we have developed a multiphasic computational model for investigating cell mediated disc degeneration as well as exploring new strategies for disc therapies. The objective of this study was to verify this new computational model according to the guidelines of ASME V&V40. The model was discretized with finite element method and implemented in COMSOL Multiphysics. Several benchmark problems and method of manufactured solutions (MMS) were used to verify the numerical implementation. For all the benchmark problems tested, the numerical results were in excellent agreement with those analytical solutions or other numerical solutions. In addition, the observed convergence rates of primary unknowns obtained with MMS were in excellent agreement with theoretical convergence rates. This study showed that our model has been verified and found no evidence of coding errors.

Keywords: multiphasic model; intervertebral disc; verification; finite element method; method of manufactured solutions

## 1. INTRODUCTION

Degeneration of lumbar intervertebral discs (IVDs) is considered a major factor causing low back pain which ranks highest in terms of disability and costs about $100 billion per year in the United States [1]. The degeneration of intervertebral discs is a process associated with various degenerative changes in physiological metrics, including altering cell viability, hydration, glycosaminoglycan (GAG, negatively charged polysaccharide compounds) content, metabolite levels, mechanical stress/strain, electrical potential, etc [2]. These degenerative changes compromise the capacity of the disc to act as a fluid-filled cushion between adjacent vertebrae and to provide anatomical stability. It is important to quantitatively and qualitatively evaluate these degenerative changes in order to diagnose and treat disc degeneration.

Disc cells play a significant role in the pathophysiology of IVDs [2]. Recently, a cell-activity-coupled multiphasic model for human IVDs has been developed to quantify the effects of extracellular mechano-electrochemical environment on the viabilities and activities of disc cells [3,4]. This multiphasic model was based on the framework of the continuum mixture theory [5]. The rates of biochemical reactions were described with empirical relations from experiments. The cell viability was a function of the biophysical signals in the extracellular environment.

This model is capable of describing multiple biophysical phenomena associated with solid mechanics, fluid mechanics, mass transfer, swelling, electrokinetics, biochemical reactions, and cell viability in IVDs. This model has been employed to simulate the mechanical responses of disc under various loading conditions, the mass transport and biochemical reactions of metabolites and drugs, the degenerative changes in discs caused by insufficient nutrient supply, and the outcomes of cell therapy for degenerated discs [6–8]. However, the numerical implementation of the model has not been systematically verified yet. Therefore, the objective of this study was to further verify the model for simulating intervertebral disc pathophysiology. The numerical implementation of this multiphasic model was verified by using benchmark problems and the method of manufactured solutions (MMS).

## 2. MODEL AND IMPLEMENTATION

### 2.1 Multiphasic Model

Based on the continuum mixture theory [5,9], the IVD is modeled as a mixture consisting of solid phase with constituents of non-charged macromolecules, negatively charged GAG, and cells, fluid phase (interstitial water), and solute phase with multiple species (such as $Na^+$, $Cl^-$, oxygen, glucose, lactate, etc).

[1] Contacting Author: wgu@miami.edu

In this paper, constituents are generically denoted by superscript $\alpha$, solid, fluid, and solute phases are denoted by superscript $s$, $w$, and $i$, respectively.

The mass balance equation for constituent $\alpha$ in the current configuration is given by,

$$\frac{\partial \rho^{\alpha}}{\partial t} + \nabla \cdot (\rho^{\alpha} \boldsymbol{v}^{\alpha}) = \hat{\rho}^{\alpha}, \tag{1}$$

where $\rho^{\alpha}$ is the apparent mass (or a quantity proportional to mass) density (per unit mixture volume) of constituent $\alpha$, $\boldsymbol{v}^{\alpha}$ is the velocity of constituent $\alpha$, and $\hat{\rho}^{\alpha}$ is the source term representing the rate of mass supply to constituent $\alpha$ from constituents other than $\alpha$. The mass is conserved over all constituents in the mixture, thus the source terms are constrained with $\sum \hat{\rho}^{\alpha} = 0$. The apparent density $\rho^{\alpha}$ is related to the true density $\rho_T^{\alpha}$ via $\rho_T^{\alpha} = \phi^{\alpha}\rho^{\alpha}$, where $\phi^{\alpha}$ is the volume fraction (constituent volume over mixture volume) of constituent $\alpha$ in the mixture. With the assumptions that mixture is fully saturated and each constituent is intrinsically incompressible, it follows that $\sum \phi^{\alpha} = 1$, and

$$\nabla \cdot (\sum \phi^{\alpha} \boldsymbol{v}^{\alpha}) = \sum \frac{\hat{\rho}\alpha}{\rho_T^{\alpha}}. \tag{2}$$

The above equation can be simplified with the assumptions that the volume fraction of solute is negligible (i.e., $\phi^s + \phi^w \approx 1$) and mass supply due to chemical reactions have negligible contribution to total mixture volume change over time (i.e., $\sum \frac{\hat{\rho}\alpha}{\rho_T^{\alpha}} \approx 0$). Then, the mass balance equation for the mixture can be reduced to,

$$\nabla \cdot (\boldsymbol{v}^s + \boldsymbol{j}^w) = 0\ , \tag{3}$$

where $\boldsymbol{j}^w = \phi^w(\boldsymbol{v}^w - \boldsymbol{v}^s)$ is the volumetric flux of fluid phase relative to the solid phase.

For each constituent in the solid phase, denoted by superscript $s*$, the mass balance equation can be rewritten, with the fact that $\boldsymbol{v}^{\alpha} = \boldsymbol{v}^s$, as,

$$\frac{\partial \rho^{s*}}{\partial t} + \nabla \cdot (\rho^{s*} \boldsymbol{v}^s) = \hat{\rho}^{s*}\ . \tag{4}$$

With the assumption that the biochemical reactions have a negligible effect on the total mass of solid phase, the mass balance equation for the solid phase may be written as,

$$\phi^s = \frac{\phi_0^s}{J}, \tag{5}$$

where $\phi_0^s$ is the volume fraction of solid phase in the reference configuration, and $J$ represents det (**F**) (where **F** is the deformation gradient of the mixture).

For solutes, the mass balance equation (eq. 1) may be expressed in terms of molar concentration (per fluid volume) as,

$$\frac{\partial(\phi^w c^i)}{\partial t} + \nabla \cdot \left(\boldsymbol{j}^i + \phi^w c^i \boldsymbol{v}^s\right) = \phi^w \hat{c}^i, \tag{6}$$

with

$$c^i = \frac{\rho^i}{\phi^w M^i}, \qquad \hat{c}^i = \frac{\hat{\rho}^i}{\phi^w M^i}, \tag{7}$$

and

$$\boldsymbol{j}^i = \phi^w c^i \left(\boldsymbol{v}^i - \boldsymbol{v}^s\right), \tag{8}$$

where $c^i$ is the molar concentration of solute $i$, $\boldsymbol{j}^i$ is the molar flux of solute $i$ (relative to solid phase), $\hat{c}^i$ is a source term, $M^i$ is the molar weight of solute $i$, and $\boldsymbol{v}^i$ is the velocity of solute $i$.

The electroneutrality condition is assumed to apply at every point in the mixture. Thus, the summation of electrical charges over all constituents should be zero, that is,

$$\sum z^i c^i - c^F = 0\ , \tag{9}$$

where $z^i$ is the valence of solute $i$, $c^F$ is the fixed charge density. In the IVD, the fixed charge density may be estimated by,

$$c^F = \frac{2\rho^{GAG}}{\phi^w M^{GAG}}, \tag{10}$$

where $\rho^{\mathrm{GAG}}$ and $M^{GAG}$ are the apparent mass density and molar weight of GAG, respectively.

The linear momentum balance equation for the mixture at quasi-static condition is,

$$\nabla \cdot \boldsymbol{\sigma} = \mathbf{0}\ , \tag{11}$$

where $\boldsymbol{\sigma}$ is the total Cauchy stress for the mixture. Note that the momentum supply due to chemical reactions and the body forces are ignored in equation (11). The total Cauchy stress can be written as,

$$\boldsymbol{\sigma} = -p\boldsymbol{I} + \boldsymbol{\sigma}^{\mathrm{e}}, \tag{12}$$

where $p$ is the fluid pressure, $\boldsymbol{I}$ is the identity tensor, and $\boldsymbol{\sigma}^{\mathrm{e}}$ is the stress due to solid phase deformation. The solid phase may be modeled as a hyperelastic material, then $\boldsymbol{\sigma}^{\mathrm{e}}$ can be evaluated via

$$\boldsymbol{\sigma}^{\mathrm{e}} = \frac{1}{J}\frac{\partial W}{\partial \boldsymbol{F}}\boldsymbol{F}^T, \tag{13}$$



 

where $W$ is the strain energy density function, and again, $\boldsymbol{F}$ is the deformation gradient tensor. The strain energy density may be a function of deformation gradient ($\boldsymbol{F}$), initial solid volume fraction ($\phi_0^s$), anisotropic structure tensor, damage state, and temperature.

The fluid and solute fluxes are driven by the gradients of (electro)chemical potentials of fluid and solutes, which can be written as,

$$\boldsymbol{j}^w = -RT\boldsymbol{k}\left(\nabla\varepsilon^w + \sum \boldsymbol{h}^i \frac{c^i}{\varepsilon^i}\nabla\varepsilon^i\right), \tag{14}$$

$$\boldsymbol{j}^i = \boldsymbol{h}^i c^i \boldsymbol{j}^w - \frac{\phi^w c^i}{\varepsilon^i}\boldsymbol{d}^i\nabla\varepsilon^i, \tag{15}$$

with

$$\varepsilon^w = \frac{p}{RT} - \varphi\sum c^i, \tag{16}$$

$$\varepsilon^i = \gamma^i c^i e^{\frac{z^i F_c \psi}{RT}}, \tag{17}$$

where $R$ is the universal gas constant, $T$ is the absolute temperature, $\boldsymbol{k}$ is the hydraulic permeability tensor, $\boldsymbol{h}^i$ is the convection coefficient tensor for solute $i$, $\boldsymbol{d}^i$ is the diffusion coefficient tensor, $\varphi$ is the overall osmotic coefficient, $\gamma^i$ is the activity coefficient of solute $i$, $F_c$ is the Faraday constant, $\psi$ is the electrical potential, and $\varepsilon^w$ and $\varepsilon^i$ are modified (electro)chemical potentials for fluid and solutes [10], respectively.

### 2.2 Finite Element Implementation

The finite element method is used to discretize the multiphasic model. The computational domain is defined on the solid phase. The primary unknown variables for numerical analysis are displacement vector for solid phase ($\boldsymbol{u}$), apparent mass density for solid constituent ($\rho^{s*}$), modified chemical potential for the fluid phase ($\varepsilon^w$), and modified electro-chemical potential for solutes ($\varepsilon^i$).

Dirichlet boundary conditions are prescribed for these primary unknown variables on the boundary where their values are known. Neumann boundary conditions are prescribed on the boundary where traction, $\boldsymbol{\sigma}\cdot\boldsymbol{n}$, fluid flux, $\boldsymbol{j}^w\cdot\boldsymbol{n}$, and solute flux, $\boldsymbol{j}^i\cdot\boldsymbol{n}$ are given (where $\boldsymbol{n}$ is the outward unit normal vector on the boundary). Note that no boundary conditions are needed for $\rho^{s*}$.

The governing equations (eqs. 3, 4, 6 and 11) in the current configuration may be transformed back to the reference configuration for discretization. For example, the stress and fluxes in equations (13-15) can be transformed into the reference configuration with the following identities,

$$\boldsymbol{P} = J\boldsymbol{\sigma}\boldsymbol{F}^{-T}\ ,\quad \boldsymbol{J}^w = J\boldsymbol{F}^{-1}\boldsymbol{j}^w\ ,\ \boldsymbol{J}^i = J\boldsymbol{F}^{-1}\boldsymbol{j}^i\ , \tag{18}$$

where $\boldsymbol{P}$ is the first Piola-Kirchhoff stress tensor, $\boldsymbol{J}^w$ and $\boldsymbol{J}^i$ are the fluid volume flux and solute molar flux in the reference configuration, respectively.

The primary unknowns are discretized and approximated with Lagrange interpolations. The order of interpolation is determined by the governing equations. The mass balance equations for the mixture (eq. 3) and for solutes (eq. 6) show that the solid velocity, fluid flux, and solute flux should have the same order of interpolation, which indicates that the modified (electro)chemical potentials for fluid and solute should be interpolated one order higher than the displacement of solid (see eqs. 14-17). The linear momentum equation for the mixture (see eqs. 12 and 13) shows that the solid stress and fluid pressure should have the same order of interpolation, which indicates that the displacement of solid should be interpolated one order higher than the modified (electro)chemical potentials. The mass balance and linear momentum balance equations indicate conflict interpolation strategies. We decided to take second order interpolation for solid displacement and first order for modified (electro)chemical potentials because this strategy can effectively reduce numerical oscillations. There is no strict restriction to the order of interpolation for $\rho^{s*}$, so we used the discontinuous Lagrange interpolation of order zero to reduce the computational cost.

We implemented the finite element model into the commercial software COMSOL Multiphysics (Version 5.4, COMSOL, MA) using the weak form module. We implemented each primary unknown separately so that we can easily disable some primary unknowns in the simulations if we want to run a model with reduced number of phases. For example, we can use this implementation to simulate finite deformation of a hyperelastic material by disabling the primary unknowns other than the solid displacement. The implicit backward differentiation formula (BDF) method was used for time stepping and all the primary unknowns were fully coupled in calculations.

Table 1 List of benchmark problems.

| Benchmark Problems | Biophysical Fields | Phases |
|---|---|---|
| large deformation of beam in bending | solid mechanics | solid phase |
| creep of confined biphasic material | solid mechanics, fluid mechanics | solid phase, fluid phase |
| free swelling of confined triphasic material under osmotic loading | solid mechanics, fluid mechanics, mass transfer, swelling, electrokinetics | solid phase (with charged constituents), fluid phase, solute phase |
| biochemical reaction and transport | mass transfer, biochemical reactions | solute phase |



 

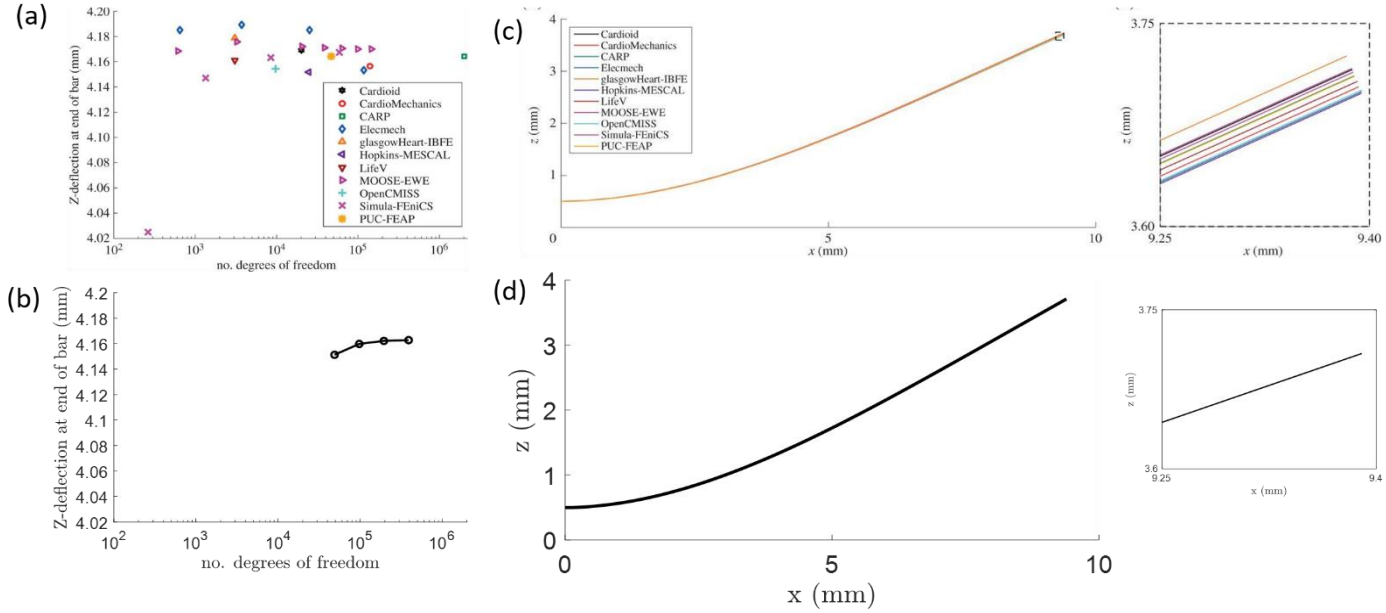


**Figure 1:** Simulation results for large deformation of a beam in bending. (a) deformed displacement at the point (10, 0.5, 1) vs. the number of degrees of freedom in the literature [11]; (b) our simulated result at the same location; (c) deformed location of the line (x, 0.5, 0.5) in [11]; and (d) our simulated result with 194,643 degrees of freedom. (a) and (c) were obtained from [11] under Creative Commons Attribution License.

## 3. VERIFICATION

Considering the complexity of the biophysical couplings among multiple phases (or constituents), several benchmark problems (Table 1) were used to verify the numerical implementation for the cases where the governing equations (or biophysical fields) were partially coupled, and the method of manufactured solutions (Table 2) was used to verify the numerical implementation of fully coupled governing equations.

### 3.1 Verification with Benchmark Problems

#### 3.1.1. Large Deformation of Beam in Bending

The deformation of a rectangular beam under mechanical loading was simulated to verify the implementation of the governing equation (eq. 11) related to solid phase deformation. The undeformed beam was in the region $x \in [0,10]$ , $y \in [0,1]$, $z \in [0,1]$ mm. The beam material was incompressible and transversely isotropic with fiber in the x-direction. One end $(x = 0)$ of the beam was fixed in all directions and a pressure of 4 Pa is applied to the entire bottom face ($z = 0$). The strain energy density function was assumed to be,

$$W = \frac{c}{2}(e^{Q} - 1) + \frac{\lambda}{2}(\ln J)^2 , \tag{19}$$

with

$$Q = b_f E_{11}^2 + b_t(E_{22}^2 + E_{33}^2 + E_{23}^2 + E_{32}^2) + b_{fs}(E_{12}^2 + E_{21}^2 + E_{13}^2 + E_{31}^2) , \tag{20}$$

where $E_{ij}$ were components of the Green-Lagrange strain tensor $\boldsymbol{E}$ in a local orthonormal coordinate system with fibers in the $e_1$-direction, and $c$, $b_f$, $b_t$, $b_{fs}$, $\lambda$ were the material parameters. In this simulation, the material parameters were chosen to be $c = 2$kPa, $b_f = 8$, $b_t = 2$, $b_{fs} = 4$. The value of $\lambda$ was chosen sufficiently high to satisfy near-incompressibility.

The verification was carried out through comparing our simulation results to the simulation results provided by other researchers [11]. Our simulated result for the deformed location originally at the point (10, 0.5, 1) converged to 4.16 mm as the number of degrees of freedom increases (Fig. 1b), which confirmed mesh convergence for this problem. Our simulated result (Fig. 1d) for the deformed location of the central line originally in (x, 0.5, 0.5) was in excellent agreement with that in the literature [11].

#### 3.1.2. Creep of Confined Biphasic Material

The creep deformation of a sample of biphasic material confined in a rigid chamber with impermeable bottom and side walls was simulated to verify the implementation of equations (3) and (11), which was related to mechanical couplings between solid and fluid phases. The top surface of the sample was compressed with a constant load applied via a free-draining rigid porous plate. The sample was a cylinder with 0.1 m in radius and 0.1 m in height. The solid phase was modeled as a hyperelastic St. Venant-Kirchhoff elastic material:

$$W = \frac{1}{2}\lambda(\mathrm{tr}\,\boldsymbol{E})^2 + \mu(\boldsymbol{E}:\boldsymbol{E}) , \tag{21}$$

where $\lambda$ and $\mu$ were the Lame constants, and $\boldsymbol{E}$ was the Green-Lagrange strain tensor. In the simulation of this benchmark problem, the material parameters were chosen to be $\lambda = 0.4$ MPa and $\mu = 0.3$ MPa, and the hydraulic permeability of the sample was chosen to be $k = 3 \times 10^{-12} \frac{\mathrm{m}^4}{\mathrm{N \cdot s}}$. The applied load (stress) was chosen to be 5 kPa, and fluid pressure at the top surface was set to zero. The geometry was meshed with hexahedral elements, and the mesh was refined by increasing element number along height direction. The simulated displacement at the top surface as a function of the element number was shown in Figure 2a, which confirmed mesh convergence for this problem. Figure 2b showed that our simulated displacement at top surface, with 10 elements along height direction, was in excellent agreement with its analytical solution (see eq.A1) [12].

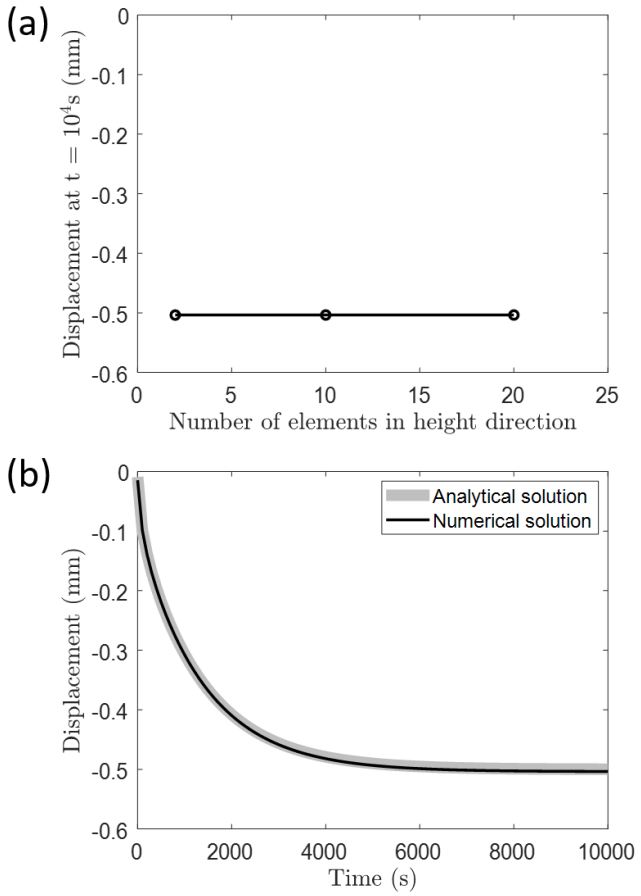


**Figure 2:** Simulated results for creep of a confined biphasic material. (a) mesh convergence results; (d) comparison of simulated result to analytical solution in [12].

### 3.1.3. Swelling of Confined Triphasic Material Under Osmotic Loading

The swelling of a charged and hydrated tissue under osmotic loading was simulated to verify the implementation of equations (3), (6), and (11), which was related to mechano-electrochemical couplings among charged solid, fluid, and solute phases. The tissue was initially equilibrated in 0.15 M saline solution with a cubic shape ($0.5 \times 0.5 \times 0.5$ mm). It was confined in a rigid chamber of the same size with impermeable walls at the bottom and four sides. The solid phase was also modeled as a hyperelastic St. Venant-Kirchhoff elastic material. The material parameters were set to the same values in Sun et al. [10], i.e., $\lambda = 0.3$ MPa, $\mu = 0.1$ MPa, $k = 1.07 \times 10^{-15} \frac{\mathrm{m}^4}{\mathrm{N \cdot s}}$, $D^+ = 0.5 \times 10^{-9} \frac{\mathrm{m}^2}{\mathrm{s}}$, $D^- = 0.8 \times 10^{-9} \frac{\mathrm{m}^2}{\mathrm{s}}$, $\phi_0^w = 0.75$, $c_0^F = 0.2$ M, $T = 298$ K. The initial equilibrium free swelling state was chosen as the reference configuration for this problem. In this swelling test, the bath solution concentration dropped to 0.125 M in 10 s and then remained to be constant. Fluid pressure in bath was set to zero. In our simulation, the chemical potential of fluid phase and electrochemical potential of solute phase were continuous across the top surface. The geometry was meshed with hexahedral elements, and the mesh was refined by increasing element number along height direction. The simulated strain at top surface versus number of elements along height direction is shown in Figure 3a, which confirmed mesh convergence for this problem. Figure 3b showed that our simulated strain at the top surface, with 50 elements along height direction, was in excellent agreement with finite difference solution in [10].

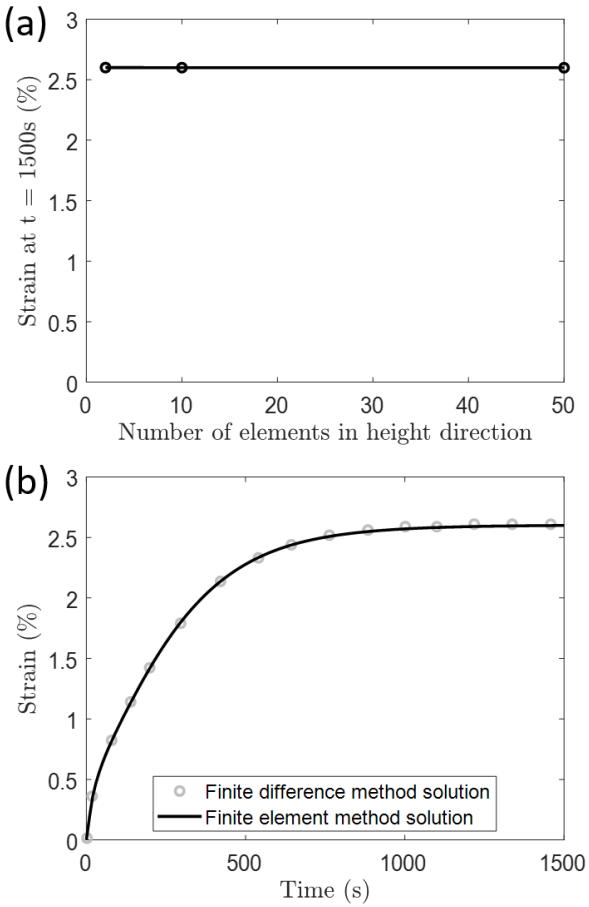


**Figure 3:** Simulation results for the free-swelling of a confined triphasic material. (a) mesh convergence results; (b) comparison of simulation result to finite difference solution in [10]

### 3.1.4. Mass Transport and Biochemical Reactions

A case of cartilage matrix synthesis and spatial variation of matrix products presented in [13] was simulated to verify the implementation of equations related to mass transport and biochemical reactions. In this case, matrix products were assumed to be distributed among three pools: soluble/free (f), bound (b), and degraded (d). Products in the soluble and degraded pools were mobile via diffusion. The governing equations presented in [13] are equivalent to our equations (4) and (6). Specifically, equation (6) can be used to describe soluble pool and degraded pool with,

$$\hat{c}^f = k^f - r^b, \tag{22}$$

$$\hat{c}^d = r^d\,, \tag{23}$$

where $k^f$ was the matrix formation rate, $r^b$ was the matrix binding rate, $r^d$ was the matrix degradation rate; and equation (4) could be used to describe bound pool with,

$$\hat{\rho}^b = r^b - r^{\mathrm{d}}. \tag{24}$$

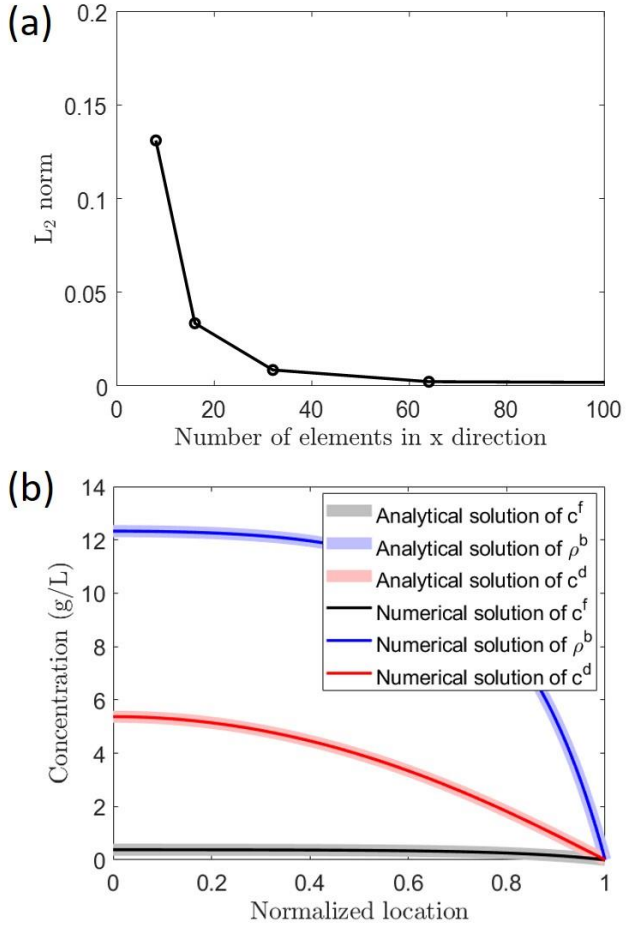


**Figure 4:** Simulation results for a problem with biochemical reaction and mass transport. (a) mesh convergence results; (b) comparison of simulated solutions to analytical solutions in [13].

An analytical solution was given for one-dimensional spatial distribution of matrix products at steady state in [13]. This analytical solution was used to verify our implementation, and the L2 norm was used to evaluate the difference between analytical solutions and simulated solutions. In our simulation, we used a three-dimensional beam geometry ($x \in [0, 1]$ , $y \in [-0.1, 0.1]$ , $z \in [-0.1, 0.1]$ mm) to represent the tissue. Concentration boundary conditions were prescribed at one end ($x = 1$), and symmetry conditions were prescribed at other boundaries. Though we use a three-dimensional geometry in our simulation, the solutions should only vary in the x-direction with the setting of boundary conditions. Values of parameters were chosen to be the same as those in Table II of [13]. The geometry was meshed with hexahedral elements, and the mesh was refined by increasing element number along the x-direction. The L2 norm decreased with increasing element number (Fig. 4a) which confirmed mesh convergence for this problem. Excellent agreement was achieved between the analytical solutions (see eq.A2) and the simulated solutions (Fig. 4b).

### 3.2 Verification with MMS

We used the MMS to verify the implementation of all governing equations that may be used to simulate the pathophysiology of IVDs. These governing equations represented the full couplings among solid phase (including GAG and cells), fluid phase, and solute phase (including $Na^+$, $Cl^-$, oxygen, glucose, and lactate) in the IVD. Equations (3) and (11) are for the mixture, equation (4) is for GAG and cells, and equation (6) is for $Na^+$, $Cl^-$, oxygen, glucose, and lactate. In MMS, these partial differential equations (PDEs) are represented with a generic system of PDEs [14],

$$D(\boldsymbol{\psi}) = 0\,, \tag{25}$$

where $D(\cdot)$ is a differential operator, and $\boldsymbol{\psi}$ is a vector of unknown variables. A differential function $\tilde{\boldsymbol{\psi}}$ is manufactured to describe the variation of variables in time and space. A corresponding source term, $\boldsymbol{S}_\psi$, is also manufactured by taking $\tilde{\boldsymbol{\psi}}$ into equation (25),

$$D(\tilde{\boldsymbol{\psi}}) = \boldsymbol{S}_\psi. \tag{26}$$

The above equation not only has all the same differential terms as equation (25), but also has an exact solution. Thus, solving equation (26) with given $\boldsymbol{S}_\psi$ can verify the implementation of equation (25).

In this verification, the domain was a cylinder with height $h =$ 1 m, and radius $r =$ 1.5 m. The cylinder was defined in a cartesian coordinate system and the origin of the coordinate system was placed in the center of the inferior surface of the cylinder. The manufactured solutions are listed in Table 2.

Source terms were computed with equation (26). Boundary conditions were evaluated from the manufactured solutions at the boundary surfaces of the problem domain. Initial conditions were also evaluated from manufactured solutions by setting $t =$



 

0s. The problem domain was discretized with tetrahedral mesh, and a series of four meshes (with different mesh sizes) were used in the verification study. The mesh size, $H$, was characterized with the averaged value of length of each element's longest edge. The discretization error between manufactured solutions and computed solutions at $t = t_0$ were evaluated using the L2 norm. Simulation results showed that the observed convergence rates were in excellent agreement with the theoretical convergence rates (Fig. 5), which confirmed the correctness of code implementation.

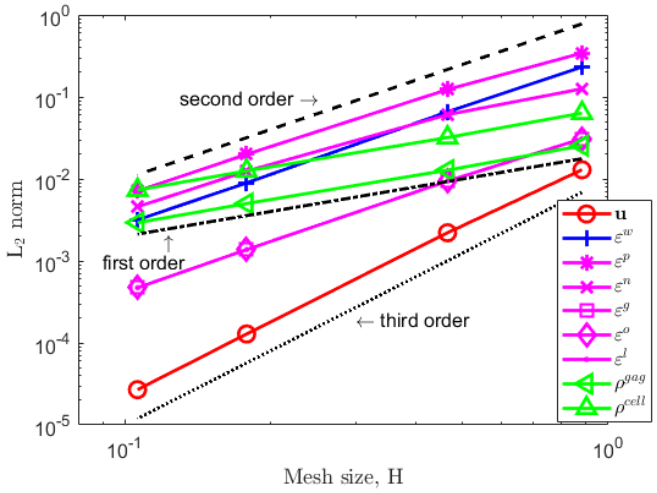


**Figure 5:** Log-log plot of L2 norm versus mesh size.

## 4. DISCUSSION AND CONCLUSION

Our multiphasic model for simulating the pathophysiology of IVDs covers multiple aspects of tissue behaviors and phenomena, such as tissue swelling, solute transport, metabolism of nutrients, cell viability, electrical signals and biomechanics. The code of the model has been verified with available benchmark problems as well as MMS.

The results of numerical simulations were in excellent agreement with analytical or other numerical solutions for all benchmark problems. With MMS, we have confirmed that the observed convergence rates for these primary unknows were consistent with theoretical convergence rates. This thoroughly verified model ensures the numerical accuracy of our model, which is important for simulating IVD degeneration, for understanding IVD pathophysiology, as well as for in-silico clinical trials for disc therapy.

## APPENDIX

The analytical solution for the benchmark problem in Section 3.1.2 is [12]:

$$u(t) = -\frac{\sigma_0}{H_A}\left\{h - \frac{2h}{\pi^2}\sum_{n=0}^{\infty}\frac{(-1)^n}{\left(n+\frac{1}{2}\right)^2}\sin\left[\left(n+\frac{1}{2}\right)\pi\right]\exp\left(-\frac{H_A k}{h^2}\left(n+\frac{1}{2}\right)^2\pi^2 t\right)\right\}, \quad \text{(A1)}$$

where $u$ is the displacement at the top surface, $t$ is time, $\sigma_0$ is the load applied on the top surface, $h$ is the height of the sample, $H_A = \lambda + 2\mu$ is the aggregate modulus.

The analytical solution for the benchmark problem in Section 3.1.4 is [13]:

$$\begin{aligned} c^f(x') &= \frac{k^f}{r^b} f(x',\alpha), \\ \rho^b(x') &= \overline{\rho^b} + \frac{k^f}{r^d} f(x',\alpha), \\ c^d(x') &= \frac{h^2 k^f}{D^d}\left[\frac{1-x'^2}{2} - \frac{1}{\alpha^2} f(x',\alpha)\right], \end{aligned} \quad \text{(A2)}$$

with

$$x' = \frac{x}{h}, \qquad \alpha^2 = \frac{h^2 r^b}{D^f}, \qquad f(x',\alpha) = \frac{(1-e^{\alpha(1-x')})(1-e^{\alpha(1+x')})}{1+e^{2\alpha}},$$

where $h$ is the length in the x-direction, $\overline{\rho^b}$ is the value of $\rho^b$ at the $x = h$, $D^f$ and $D^d$ are the diffusivity of soluble and degraded matrix products, respectively.

**Table 2:** List of manufactured solutions.

| Manufactured Variable | Manufactured Solutions |
|---|---|
| $\tilde{\boldsymbol{u}}$ (displacement vector) | $\begin{pmatrix} 0.4\cdot\sqrt{x^2+y^2}\cdot[0.25-(z/h-0.5)^2]\cdot cos[tan^{-1}(y/x)]\cdot t/t_0 \\ 0.4\cdot\sqrt{x^2+y^2}\cdot[0.25-(z/h-0.5)^2]\cdot sin[tan^{-1}(y/x)]\cdot t/t_0 \\ -0.1\cdot x\cdot z\cdot\frac{t}{r\cdot t_0} \end{pmatrix}$ |

| | |
|---|---|
| $\widetilde{\varepsilon^{w}}$ (modified chemical potential of fluid) | $-5\cdot\{1+2\cdot[0.25-(z/h-0.5)^2]\}\cdot\left[1-\sqrt{(x/r)^2+(y/r)^2}\right]\cdot t/t_0$ |
| $\widetilde{\varepsilon^{p}}$ (modified electrochemical potential of cation) | $\{1+2\cdot[0.25-(z/h-0.5)^2]\}\cdot\left[1-\sqrt{(x/r)^2+(y/r)^2}\right]\cdot t/t_0$ |
| $\widetilde{\varepsilon^{n}}$ (modified electrochemical potential of anion) | $\{1-2\cdot[0.25-(z/h-0.5)^2]\}\cdot\left[1-\sqrt{(x/r)^2+(y/r)^2}\right]\cdot t/t_0$ |
| $\widetilde{\varepsilon^{g}}$ (modified chemical potential of glucose) | $\{1-2\cdot[0.25-(z/h-0.5)^2]\}\cdot\left[1-\sqrt{(x/r)^2+(y/r)^2}\right]\cdot t/t_0$ |
| $\widetilde{\varepsilon^{o}}$ (modified chemical potential of oxygen) | $\{1-2\cdot[0.25-(z/h-0.5)^2]\}\cdot\left[1-\sqrt{(x/r)^2+(y/r)^2}\right]\cdot t/t_0$ |
| $\widetilde{\varepsilon^{l}}$ (modified chemical potential of lactate) | $\{1+2\cdot[0.25-(z/h-0.5)^2]\}\cdot\left[1-\sqrt{(x/r)^2+(y/r)^2}\right]\cdot t/t_0$ |
| $\widetilde{\rho^{cell}}$ (cell density) | $\{1-2\cdot[0.25-(z/h-0.5)^2]\}\cdot\left[1-\sqrt{(x/r)^2+(y/r)^2}\right]\cdot t/t_0$ |
| $\widetilde{\rho^{GAG}}$ (GAG content) | $0.4\cdot\{1-2\cdot[0.25-(z/h-0.5)^2]\}\cdot\left[1-\sqrt{(x/r)^2+(y/r)^2}\right]\cdot t/t_0$ |

Note: x, y, z are the coordinates, t is time, and $t_0 = 10^5$ s.

## REFERENCES


[1] Davis, M. A., Onega, T., Weeks, W. B., and Lurie, J. D., 2012, "Where the United States Spends Its Spine Dollars," Spine (Phila. Pa. 1976).

[2] Urban, J. P. G., and Roberts, S., 2003, "Degeneration of the Intervertebral Disc," Arthritis Res. Ther., **5**(3), pp. 120–130.

[3] Zhu, Q., Jackson, A. R., and Gu, W. Y., 2012, "Cell Viability in Intervertebral Disc under Various Nutritional and Dynamic Loading Conditions: 3d Finite Element Analysis," J. Biomech., **45**(16), pp. 2769–2777.

[4] Gu, W., Zhu, Q., Gao, X., and Brown, M. D., 2014, "Simulation of the Progression of Intervertebral Disc Degeneration Due to Decreased Nutritional Supply," Spine (Phila. Pa. 1976)., **39**(24), pp. E1411–E1417.

[5] Lai, W. M., Hou, J. S., and Mow, V. C., 1991, "A Triphasic Theory for the Swelling and Deformation Behaviors of Articular Cartilage," J. Biomech. Eng., **113**(3), pp. 245–258.

[6] Zhu, Q., Gao, X., Levene, H. B., Brown, M. D., and Gu, W., 2016, "Influences of Nutrition Supply and Pathways on the Degenerative Patterns in Human Intervertebral Disc," Spine (Phila. Pa. 1976)., **41**(7), pp. 568–576.

[7] Zhu, Q., Gao, X., Brown, M. D., Eismont, F., and Gu, W., 2019, "Transport of Vancomycin and Cefepime Into Human Intervertebral Discs," Spine (Phila. Pa. 1976)., **44**(17), pp. E992–E999.

[8] Zhu, Q., Gao, X., Temple, H. T., Brown, M. D., and Gu, W., 2016, "Simulation of Biological Therapies for Degenerated Intervertebral Discs," J. Orthop. Res., **34**(4), pp. 699–708.

[9] Ateshian, G. A., Nims, R. J., Maas, S., and Weiss, J. A., 2014, "Computational Modeling of Chemical Reactions and Interstitial Growth and Remodeling Involving Charged Solutes and Solid-Bound Molecules," Biomech. Model. Mechanobiol., **13**(5), pp. 1105–1120.

[10] Sun, D. N., Gu, W. Y., Guo, X. E., Lai, W. M., and Mow, V. C., 1999, "A Mixed Finite Element Formulation of Triphasic Mechano-Electrochemical Theory for Charged, Hydrated Biological Soft Tissues," Int. J. Numer. Methods Eng., **45**(10), pp. 1375–1402.

[11] Land, S., Gurev, V., Arens, S., Augustin, C. M., Baron, L., Blake, R., Bradley, C., Castro, S., Crozier, A., Favino, M., Fastl, T. E., Fritz, T., Gao, H., Gizzi, A., Griffith, B. E., Hurtado, D. E., Krause, R., Luo, X., Nash, M. P., Pezzuto, S., Plank, G., Rossi, S., Ruprecht, D., Seemann, G., Smith, N. P., Sundnes, J., Rice, J. J., Trayanova, N., Wang, D., Jenny Wang, Z., and Niederer, S. A., 2015, "Verification of Cardiac Mechanics Software: Benchmark Problems and Solutions for Testing Active and Passive Material Behaviour," Proc. R. Soc. A Math. Phys. Eng. Sci., **471**(2184), p. 20150641.

[12] Mow, V. C., Kuei, S. C., Lai, W. M., and Armstrong, C. G., 1980, "Biphasic Creep and Stress Relaxation of Articular Cartilage in Compression: Theory and Experiments," J. Biomech. Eng., **102**(1), p. 73.

[13] Dimicco, M. A., and Sah, R. L., 2003, "Dependence of Cartilage Matrix Composition on Biosynthesis, Diffusion, and Reaction," Transp. Porous Media, **50**(1–2), pp. 57–73.

[14] Shunn, L., and Ham, F., 2007, "Method of Manufactured Solutions Applied to Variable Density Flow Solvers"," Cent. Turbul. Res., pp. 155–167.




 